

Measurement of the spatiotemporal dynamics of simple transverse patterns in a pulsed transversely excited atmospheric CO₂ laser

F. Encinas-Sanz, Oscar G. Calderón,* R. Gutiérrez-Castrejón, and J. M. Guerra

Departamento de Óptica, Facultad de Ciencias Físicas, Universidad Complutense de Madrid, Ciudad Universitaria s/n, 28040 Madrid, Spain

(Received 13 August 1998)

A study of the spatiotemporal evolution of a pulsed CO₂ laser is performed using an experimental setup which allows transverse pattern recordings with 1-ns resolution. A rich laser dynamics, hidden until now behind temporal averages, is uncovered. Features like spontaneous symmetry breaking, mode beating, and phase locking are observed and theoretically interpreted using Maxwell-Bloch equations. Numerical simulations by means of mode decompositions are performed, showing very good agreement with the empirical results. The influence of the curvature of the mirrors in the dynamics of the system is also theoretically analyzed. [S1050-2947(99)05806-0]

PACS number(s): 42.65.Sf, 42.55.Lt, 02.60.Cb

I. INTRODUCTION

The study of the transient evolution of laser radiation has been a challenging problem [1]. This is mainly due to the inherent difficulty in measuring and describing such short-time-scale dynamical processes. The complexity of the problem becomes higher when one leaves the usual plane-wave approximation and pay attention to the transverse variation of the electric and magnetic fields [2–6]. From the experimental point of view, and as stressed by some authors [7], the study of the spatiotemporal dynamics in cw CO₂ has been mainly limited by the absence of a technical solution to record patterns with a temporal resolution higher than 1 μ s. Those authors are reduced to recording time-averaged patterns. The same problem arises in the measurements performed in pulsed CO₂ lasers, and hence the following question remains: What has been the “history” of transverse patterns from the beginning to the end of the laser pulse? Until now only theoretical predictions are available since, to the best of our knowledge, no direct experimental procedure has been available to check them.

From the theoretical standpoint, the solution of a system of nonlinear equations that necessarily contains time derivatives and a transverse Laplacian of the electric field demands the use of ingenious analytical and numerical techniques. When the Fresnel number of the analyzed cavity is small, the dynamics of the system can be described by the nonlinear interaction and competition among a reduced number of different transverse spatial structures (transverse modes) [3,4]. If one deals with a stable resonator with spherical mirrors, the original system of equations may be approximated by a system of coupled equations for the time-dependent amplitudes of Gauss-Hermite or Gauss-Laguerre modes [2,8]. In this paper we use the Gauss-Hermite modes, which are usually labeled by indices $n=0,1,2,\dots$ and $m=0,1,2,\dots$, and are characterized by the fact that modes with the same value of the index $(n+m)$ are frequency degenerate, provided that

a perfectly symmetric cavity is considered. On the other hand, if one is interested in the dynamics of the transverse section of a flat mirror resonator (which displays translational symmetry), a mode decomposition is not always the best choice since it is more difficult to find an analytical expression for the set of transverse mode patterns [8]. However, in a recent work we showed that it is possible to find a set formed by combination of Bessel functions which adapt well to the particular resonator geometry [9].

In this paper we will study the spatiotemporal evolution of a CO₂ laser both experimentally and theoretically. For this purpose we have developed an experimental setup that allows one to record instantaneous transverse patterns (time resolution 1 ns). The reliability of our system has been tested in the study of the time-resolved beam quality parameter of a laser beam [10]. In particular, in the present paper, we will show that the time-averaged pattern recorded during the laser pulse, that resembles a doughnutlike shape, is the consequence of a richer dynamics hidden by the average process. A theoretical analysis will be performed using Maxwell-Bloch equations for a single-longitudinal mode laser with spherical mirrors. The dynamics will be analyzed in terms of the competition among different Gauss-Hermite modes (empty cavity mode expansion) in two different ways. First, we use a modal expansion applied to the optical field [2]. Second, we propose a simple and fast method that consists of applying a modal expansion to the whole set of dynamical variables. For the sake of completeness, we have also studied the role of the curvature of the mirrors in the dynamics by means of Maxwell-Bloch equations for a flat mirror resonator. In this last case, a direct numerical simulation of equations by means of a very efficient full multigrid implementation of a linear finite-difference scheme will be performed.

In Sec. II, we describe the experimental setup used to obtain the measurements described in Sec. III. A theoretical analysis is presented in Sec. IV. In Sec. V, the effect of the curvature of mirrors is analyzed. Finally, the conclusions are given in Sec. VI.

II. EXPERIMENTAL SETUP

Our experimental setup consists of a pulsed transversely excited atmospheric CO₂ laser with an intracavity diaphragm

*Electronic address: oscargc@eucmax.sim.ucm.es

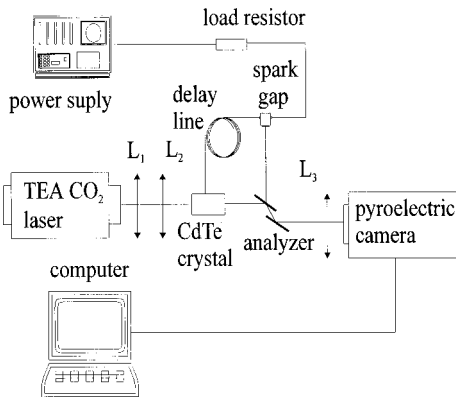


FIG. 1. Experimental setup.

that governs its Fresnel number. In this work we have used two diaphragms of diameters 8 and 11 mm. The laser cavity is a half-symmetric resonator in which the distance between the curved mirror (radius of curvature $R_1 = 10$ m and reflectivity $r_1 = 1$) and the planar output coupler (reflectivity $r_2 = 0.6$) is $L = 112$ cm. An intracavity Brewster plate has been introduced to obtain a linearly polarized beam. Our homemade laser [11] produces a $3.5\text{-}\mu\text{s}$ pulse composed of a short (60-ns width) high power gain-switch peak followed by a long quasistationary collisional transfer tail. Instantaneous measurements (the slice time width is 10 ns) of the pulse's transverse profile are obtained through a very fast, yet simple, optical switching device, which mainly consists of a CdTe crystal and a polarizer (see Fig. 1). The latter is positioned with its transmission axis perpendicular to the polarization of the beam emerging from the laser cavity. To cut such narrow time slices, a high-voltage pulse (8.48 kV) is used to produce a transverse Pockels effect in the CdTe crystal. This turns the polarization of the linearly polarized laser beam 90° . The beam is transmitted by the crossed polarizer as long as the high-voltage pulse lasts. The switching system is self-fired using a spark gap that collects the rejected light from the polarizer. The voltage pulse duration and the relative position of the time slice within the laser pulse is controlled, respectively, by the length of the coaxial pulse forming line that links the spark gap and the high-voltage charge resistor, and the length of the delay cable that links the spark gap and the switching device. The instantaneous transverse intensity pattern of the time slice is registered by a pyroelectric camera (Spiricon PYROCAM I). A reference time for each slice is measured by splitting the laser beam prior to its entrance into the electro-optical device. The complete pulse can then be collected by a fast photodetector (photon drag, 1-ns rise time), and can be compared with the chopped pulse using a digital oscilloscope. The time slice is registered by another photon drag detector that is placed for this purpose between the polarizer and the pyroelectric camera. The relative position of a time slice with respect to the pulse is illustrated in Fig. 2 for a delay of $t_0 \approx 75$ ns, measured from the beginning of the pulse.

The polarizer is based on two successive reflections under Brewster's angle, and introduces no distortion in the spatial structure of the beam profile. It also provides a secondary beam to fire the spark gap, as was previously mentioned. The telescopic system formed by lenses L_1 and L_2 avoids hard

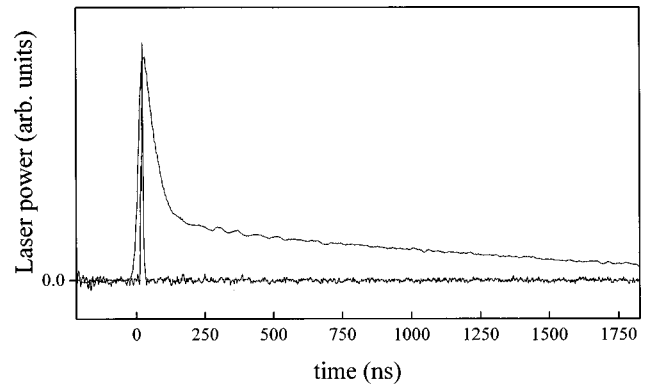


FIG. 2. Relative position of a time slice with respect to the pulse for a delay of $t_0 \approx 75$ ns, measured from the beginning of the pulse. The total pulse was filtered to eliminate the axial and transverse mode beating.

edge diffraction at the electro-optical crystal aperture by reducing the beam size through the crystal. The paraxial focal lengths of L_1 and L_2 in Fig. 1 are $f_1 = 25$ cm and $f_2 = 12.5$ cm, respectively. A third lens L_3 ($f_3 = 50$ cm) is utilized to fit the pattern size to the pyroelectric matrix dimensions.

III. MEASUREMENT OF THE INSTANTANEOUS PATTERNS

Using the above-described experimental arrangement, we studied the temporal evolution of the pulse's transverse intensity profile for two different values of the intracavity diaphragm, or, in other words, for two different Fresnel numbers $\mathcal{F} = (b/2)^2 / (\lambda L)$, where b is the diameter of the laser aperture, L the resonator length, and $\lambda = 10.6 \mu\text{m}$ the wavelength of the laser light. In the case of $\mathcal{F} \approx 1.3$ (diaphragm diameter 8 mm), a Gaussian-like (TEM_{00}) mode was registered during the whole laser pulse duration (see Fig. 3). Therefore, the time-averaged pattern during the laser pulse has the same shape (a Gaussian mode TEM_{00}) as the instantaneous patterns. In the case of $\mathcal{F} \approx 2.1$ (diaphragm diameter 11 mm), a more complex dynamics was observed. This large aperture yielded a Gaussian mode during the leading edge of the gain-switch peak [see Fig. 4(a)] followed by a deformed peak [Fig. 4(b)]. This initial transition corresponds to a situation where new transverse modes reach their oscillation threshold through a spontaneous symmetry breaking of the pattern's cylindrical symmetry. This transition was not ob-

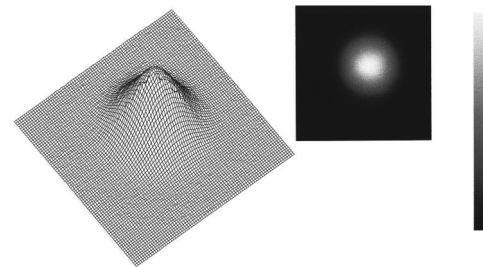


FIG. 3. Experimental transverse pattern intensity for $b = 8$ mm, at time $t \approx 2$ ns, measured from the beginning of the pulse. The real size of the picture is $8.1 \times 8.1 \text{ mm}^2$. All the figures have used the same gray scale.

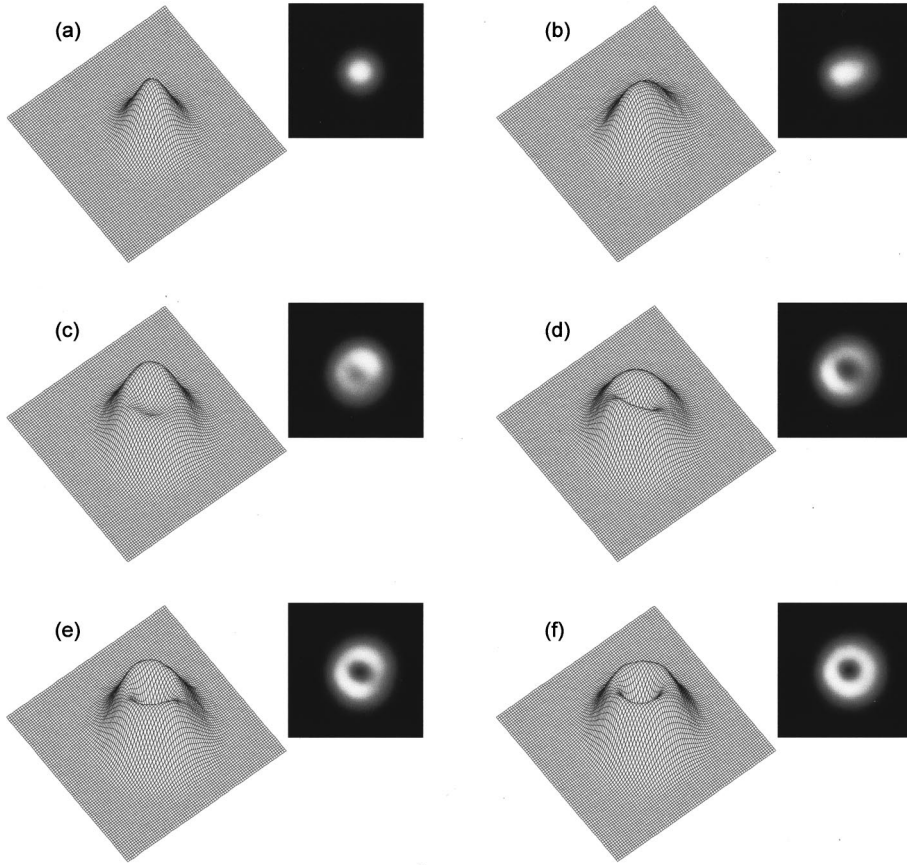


FIG. 4. Experimental transverse pattern intensity for $b = 11$ mm, at times (a) $t \approx 2$ ns, (b) $t \approx 50$ ns, (c) $t \approx 100$ ns, (d) $t \approx 200$ ns, (e) $t \approx 300$ ns, and (f) $t \approx 500$ ns, measured from the beginning of the pulse. The real size of the picture is 8.1×8.1 mm².

served in the case of a small aperture ($\mathcal{F} \approx 1.3$), as previously mentioned. After that, a shifted peak [see Fig. 4(c)] and a two symmetric peaks [see Fig. 4(d)] appear. The TEM_{00} amplitude in the two-peak pattern is continuously decreasing even when the two peaks join together to display a doughnut mode [see Figs. 4(e) and 4(f)]. This doughnut mode prevails until the end of our measurements ($1 \mu\text{s}$ approximately). Contrary to the small Fresnel number case, here the time-averaged pattern during the laser pulse is different from the instantaneous patterns. The average pattern is shown in Fig. 5. It displays a doughnutlike shape, where the field does not completely vanish in the center. The same pattern sequence was observed in several rounds of measurements, and therefore our experimental results can be replicated.

More information about the transverse mode dynamics was obtained through spatially local intensity measurements performed with the photon drag detector. In particular, a mode beating modulation shown in Fig. 6(a) was observed. Its high-resolution Fourier transform shows a peak for the beating frequency of every axial mode. Moreover, in the neighborhood of each of these axial peaks two sidebands corresponding to a transverse beating between two transverse structures can also be observed [Fig. 6(b)]. Considering the transverse contribution to the resonance frequencies of our resonator given by the empty cavity modes,

$$\nu_{nm} = \frac{c}{2\pi L} (1 + n + m) \cos^{-1} \sqrt{1 - \frac{L}{R_1}}, \quad (3.1)$$

the transverse mode beating observed correspond to two consecutive modes (14 MHz). Therefore, the recorded transverse

patterns and the frequency of the transverse mode beating clearly indicate the contribution of the TEM_{00} , TEM_{10} , and TEM_{01} modes.

IV. THEORY

A. Mode expansion

From the analysis in Sec. III, one observes that the Fourier spectrum is the same in the neighborhood of every axial beating peak [see Fig. 6(b)]. Thus the axial modes can be considered dynamically independent. Our theoretical analysis, thus, will be based upon the single-longitudinal-mode Maxwell-Bloch equations for a polarized two-level laser with spherical mirrors in the rotating wave and slowly varying amplitude approximations, which are [8,12]

$$\frac{\partial E}{\partial \tau} = ia(\Delta_{\perp} - 4\rho^2)E - \sigma E + P, \quad (4.1)$$

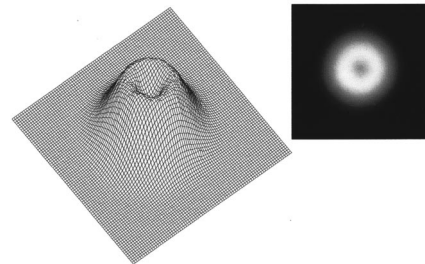


FIG. 5. Experimental time-averaged pattern intensity recorded along the laser pulse for $b = 11$ mm. The real size of the picture is 8.1×8.1 mm².

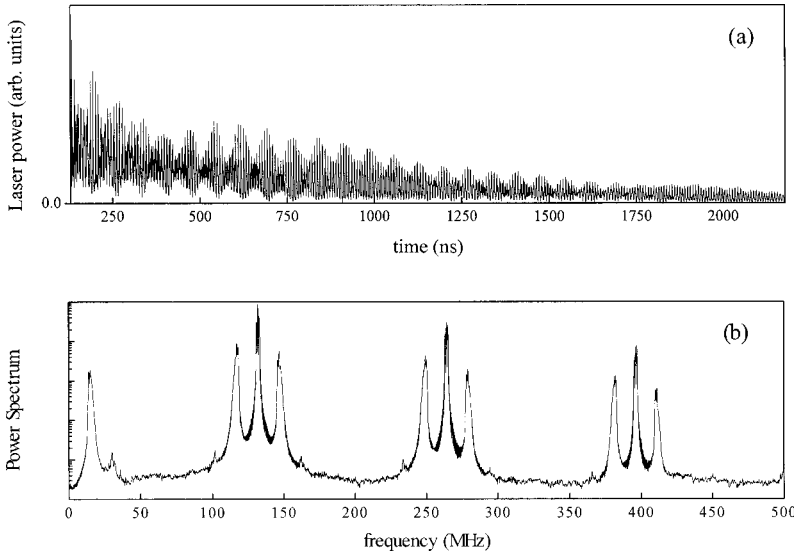


FIG. 6. (a) Time evolution of the intensity which shows the axial and transverse mode beating, and (b) the power spectrum, averaged over 100 pulses, of the intensity.

$$\frac{\partial P}{\partial \tau} = -(1 + i\Delta)P + ED, \quad (4.2)$$

$$\frac{\partial D}{\partial \tau} = -\gamma \left[D - C + \frac{1}{2}(E^*P + EP^*) \right], \quad (4.3)$$

where $\gamma = \gamma_{\parallel}/\gamma_{\perp}$ is the ratio between the relaxation rate of the population inversion and the relaxation rate of the polarization. $C = \omega_{21}\mu_{12}^2Nd_0/(2\hbar\epsilon_0\gamma_{\perp}^2)$ is a rescaled pumping, μ_{12} being the dipole moment of the transition, N the number of atoms or molecules per unit volume in the active medium, and d_0 the population inversion per atom or molecule induced by the pumping. $\Delta = (\omega_{21} - \omega)/\gamma_{\perp}$ is the rescaled detuning between the matter transition frequency and the fast oscillation of the field. $\sigma = \kappa/\gamma_{\perp}$ represents the rescaled transmission losses (κ is the relaxation time constant of the field) including mirror coupling, internal transmission losses, aperture diffraction, etc. $a = \lambda c/(4\pi\gamma_{\perp}w_0^2)$ is the diffraction coefficient, where $w_0 = \lambda\sqrt{L(R_1 - L)}/\pi$ is the minimum beam waist. The transverse coordinates are scaled to the minimum beam waist, $(\xi, \eta) = (x, y)/w_0$. $\Delta_{\perp} = \partial_{\xi}^2 + \partial_{\eta}^2$ is the transverse Laplacian, and the term $-ia4\rho^2E$, where $\rho^2 = \xi^2 + \eta^2$ is the radial transverse coordinate, represents the phase shift induced by the presence of the spherical mirror. The rescaled time variable is $\tau = \gamma_{\perp}t$. Here E , P , and D are the dimensionless envelopes of the electric field, the electric polarization and the population inversion. They are scaled by the following factors, respectively: $\hbar\sqrt{\gamma_{\perp}\gamma_{\parallel}}/(2\mu_{12})$, $-i\mu_{12}\sqrt{\gamma_{\perp}\gamma_{\parallel}}/(c\sigma_{21})$, and $2\gamma_{\perp}/(c\sigma_{21})$, where σ_{21} is the material cross section given by $\sigma_{21} = \mu_{12}^2\omega/(\hbar\epsilon_0c\gamma_{\perp})$.

In this section, we will use the standard Gauss-Hermite mode expansion technique of the optical field to simplify the above-mentioned system of laser equations [2,8,12]. In agreement with the experimental observations, we will consider the situation in which only the first three modes (0,0), (1,0), and (0,1) are active. According to our resonator specifications ($L = 1.12\text{m}$, $R_1 = 10\text{m}$, and $R_2 = \infty$), since $R_1 \gg L$, the spot size of the beam [$w(z)$, where z is the longitudinal coordinate] can be considered approximately constant along the longitudinal axis $w^2 \approx w_0^2 \approx \lambda\sqrt{R_1L}/\pi$, that is, the Ray-

leigh length of the cavity is much larger than the resonator length ($z_0 = \pi w(0)^2/\lambda \gg L$). Therefore, the mode functions can be written as

$$A_0(\xi, \eta) = \sqrt{\frac{2}{\pi}} \exp(-\rho^2) \quad (4.4)$$

for the fundamental cylindrical symmetric mode TEM_{00} ($n = 0$, $m = 0$), and

$$A_1(\xi, \eta) = 2\eta A_0(\xi, \eta), \quad (4.5)$$

$$A_2(\xi, \eta) = 2\xi A_0(\xi, \eta) \quad (4.6)$$

for the modes TEM_{01} ($n = 0$, $m = 1$), and TEM_{10} ($n = 1$, $m = 0$), respectively. The most general expression for the slowly varying envelope of the electric field operating on these modes is

$$E(\xi, \eta, \tau) = \sum_{j=0}^2 A_j(\xi, \eta) e_j(\tau). \quad (4.7)$$

We insert expansion (4.7) into Eqs. (4.1)–(4.3) to obtain

$$\frac{\partial e_j}{\partial \tau} = -i\Omega_j e_j - \sigma_j e_j + \int d\vec{\rho} A_j P, \quad (4.8)$$

$$\frac{\partial P}{\partial \tau} = -(1 + i\Delta)P + ED, \quad (4.9)$$

$$\frac{\partial D}{\partial \tau} = -\gamma \left[D - C + \frac{1}{2}(E^*P + EP^*) \right]. \quad (4.10)$$

$\Omega_0 = c/(\gamma_{\perp}\sqrt{LR_1})$ and $\Omega_1 \equiv \Omega_2 = 2c/(\gamma_{\perp}\sqrt{LR_1})$, where using the transverse contribution to the resonance frequencies [Eq. 3.1] $\Omega_0 \approx \omega_{00}/\gamma_{\perp}$ and $\Omega_1 \equiv \Omega_2 \approx \omega_{01}/\gamma_{\perp} (\approx \omega_{10}/\gamma_{\perp})$, with ω_{00} , ω_{01} , and ω_{10} the usual transverse frequencies of the three lowest order transverse modes in the resonator. σ_0 , σ_1 , and σ_2 are the total losses for the TEM_{00} , TEM_{01} , and TEM_{10} modes, respectively.

The loss profile has been considered flat near the optical axis, and mainly due to mirror losses $\kappa_{\text{in}} \approx 1/(2t_c)$

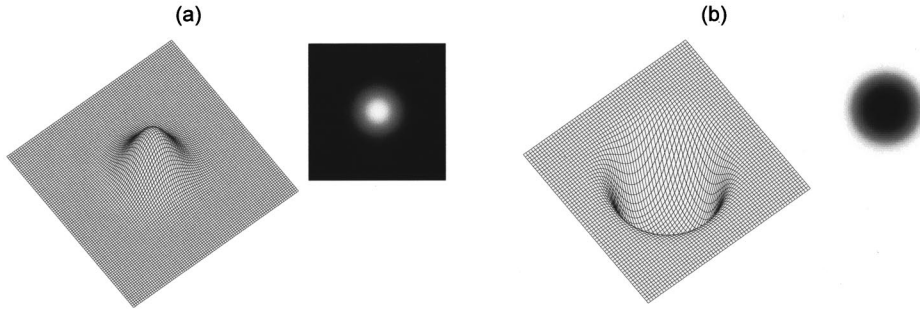


FIG. 7. Calculated transverse pattern (a) intensity, and (b) population inversion for $b=8$ mm, at $\tau=600$. The real size of the picture is $5w_0 \times 5w_0$.

$=L/(2c \ln(\sqrt{r_1 r_2}))$. Outside this area the losses are mainly due to diffraction in diaphragm edges. We simulate that strong losses by a Fermi-like function distribution in the radial direction,

$$F(\rho) = 1 - \frac{1}{1 + \exp[p(b)(\rho - h(b))]}, \quad (4.11)$$

$$\kappa = \kappa_{\text{in}} + \kappa_{\text{out}} F(\rho), \quad (4.12)$$

where we take $\kappa_{\text{out}} \approx 100\kappa_{\text{in}}$.

Therefore, the corresponding losses for each mode are

$$\sigma_j = \frac{\kappa_{\text{in}}}{\gamma_{\perp}} + \frac{\kappa_{\text{out}}}{\gamma_{\perp}} \int d\rho F(\rho) A_j(\xi, \eta). \quad (4.13)$$

The pumping has been assumed to be flat in the transverse plane (in agreement with the highly uniform glow discharge that pump the laser) and time dependent with a fast rise time followed by a slow exponential decay (the maximum value at the top of the pulse is $C_0=1.4$). According to the geometrical parameters of our resonator, we have $\kappa_{\text{in}}=3.4 \times 10^7 \text{ s}^{-1}$, $\kappa_{\text{out}}=3.4 \times 10^9 \text{ s}^{-1}$, $w_0=3.36 \text{ mm}$, $\omega_{00}=90 \times 10^6 \text{ s}^{-1}$, and $\omega_{01}=\omega_{10}=180 \times 10^6 \text{ s}^{-1}$. Additionally, we have assumed the following values for the rest of the physical parameters: $\gamma_{\perp}=2 \times 10^9 \text{ s}^{-1}$, $\gamma_{\parallel}=5 \times 10^6 \text{ s}^{-1}$, and $\Delta=0.05$.

Equations (4.8)–(4.10) have been solved using finite differences in a digital computer. Several initial conditions of the fields E , P , and D have been tested, but all of them yielded a similar result to the one presented below. Then the initial value of the set of dynamical variables in all the simu-

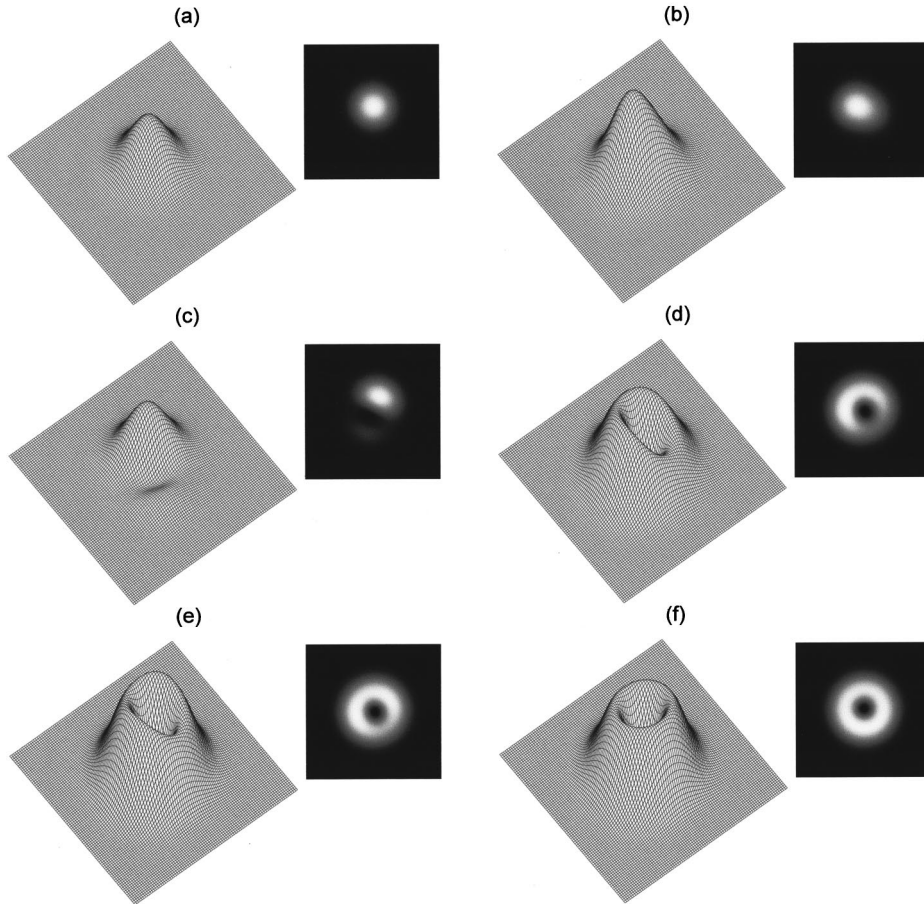


FIG. 8. Calculated transverse pattern intensity for $b=11$ mm at time (a) $\tau=200$, (b) $\tau=275$, (c) $\tau=315$, (d) $\tau=335$, (e) $\tau=410$, and (f) $\tau=615$. The real size of the picture is $5w_0 \times 5w_0$.

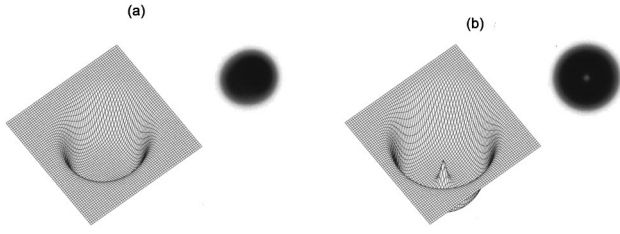


FIG. 9. Calculated transverse pattern population inversion for $b=11$ mm at time (a) $\tau \approx 300$, and (b) $\tau \approx 500$. The real size of the picture is $5w_0 \times 5w_0$.

lations presented here has been chosen as $E = (0.001 - i0.001)A_0 - (0.002 - i0.0014)A_1 + (0.0015 + i0.002)A_2$, $P=0$, and $D=0.0005(A_0^2 + A_1^2 + A_2^2)$.

Two cases are analyzed. First, a simulation with a small diameter diaphragm of $b=8$ mm ($\mathcal{F}=1.3$) is performed. Then the diameter is enlarged to $b=11$ mm ($\mathcal{F}=2.1$). In the first case the parameters of the loss function are $p=3000w_0$ and $h=b/(2w_0)$; therefore, the total losses (including the aperture losses) are $\sigma_0=0.1478$ and $\sigma_1 \equiv \sigma_2 = 0.4447$. The calculated results show that, in spite of the initial asymmetric field, only the TEM_{00} mode is present during the interaction process [Fig. 7(a)]. This is in agreement with the experimental patterns. In Fig. 7(b) we observe how the population inversion is remarkably burnt at the center. This spatial hole burning favors the TEM_{01} and TEM_{10} modes; however, the high losses of these two modes prevent them from reaching threshold and contributing to the dynamics. As a result of this the only mode above threshold is a Gaussian mode, with the following intensity distribution:

$$|E|^2 = \frac{2}{\pi} |e_0|^2 \exp(-2\rho^2). \quad (4.14)$$

In the large aperture case the parameters of the losses function are $p=450w_0$, and $h=b/w_0$, and the total losses $\sigma_0=0.0519$ and $\sigma_1 \equiv \sigma_2 = 0.0724$. According to Fig. 8(a), the Gaussian mode grows during the gain-switch peak. This is the smallest loss mode, so this is the first to appear as it happens in the experimental behavior. As in the small aperture case the population inversion is burnt at the center. The

evolution of the intensity pattern continues with a clear growing of the TEM_{01} and TEM_{10} modes, while the fundamental mode amplitude decreases. This is a consequence of the population inversion shape that favors these modes and the weaker diffraction losses that, in a large aperture cavity, the TEM_{01} and TEM_{10} modes experience. The immediate result is the cylindrical symmetry breaking of the intensity pattern [see Fig. 8(b)] that displays a deformed peak, as in the experimental measurements. As we see in Fig. 9(a), the population inversion pattern also presents a cylindrical symmetry breaking too.

When the Gaussian mode amplitude becomes smaller the intensity pattern displays a shifted peak [see Fig. 8(c)]. This is again in agreement with the experiments. We observed the rotation of the pattern in the simulated evolution [Figs. 8(c), 8(d), and 8(e)]. To explain this type of pattern by means of mode amplitudes, we define $e_1 = |e_1| \exp(i\phi_1)$ and $e_2 = |e_2| \exp(i\phi_2)$. Then the total intensity must, in principle, be given by

$$|E|^2 \approx \frac{8}{\pi} |e_1|^2 \left| \eta + \xi \frac{|e_2|}{|e_1|} \exp(i(\phi_2 - \phi_1)) \right|^2 \exp(-2\rho^2). \quad (4.15)$$

Figure 10 shows a damped oscillation of the amplitude ratio, while the phase difference tends to $\pm \pi/2$ in the same way. The oscillation of $|e_1|/|e_2|$ induces an oscillation regime in the pattern, which we will call TW2 (a traveling wave formed by two modes). As the oscillation of the amplitude ratio vanishes ($|e_2|/|e_1| \rightarrow 1$) and the phase difference goes to $\pm \pi/2$, the two peaks join together to display a doughnut mode, in agreement with the experimental pattern [see Fig. 8(f)]. The corresponding population inversion pattern is shown in Fig. 9(b). At this time the intensity is given by

$$|E|^2 \approx \frac{8}{\pi} |e_1|^2 \rho^2 \exp(-2\rho^2). \quad (4.16)$$

It can be seen in Fig. 8(f) that the corresponding doughnut mode is not a perfectly symmetrical structure. This is due to the small contribution of the TEM_{00} mode, as shown in Fig. 10(a). This is in agreement with the experimental patterns [see Fig. 4(f)].

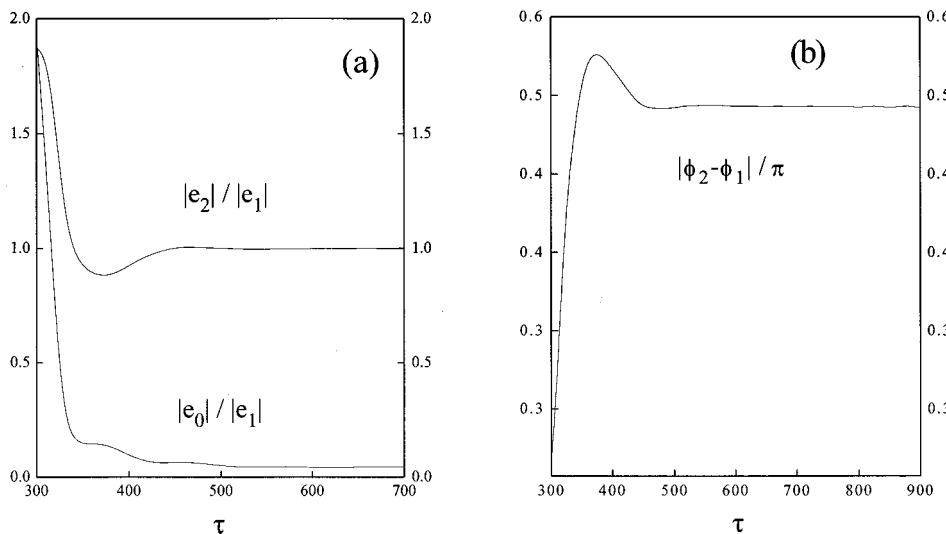


FIG. 10. (a) Amplitude ratio and (b) phase difference between the TEM_{00} , TEM_{01} , and TEM_{10} modes.

B. Expansion of the matter variables

In this section we develop a simple and fast method to study the dynamics of the system. As the Maxwell-Bloch equations (4.1)–(4.3) closely relate the matter variables P and D to the laser field E , we apply a modal expansion to the whole set of dynamical variables [13,14]. The electric field is expanded as in Sec. IV A, while the matter variables are now expanded as follows:

$$P(\xi, \eta, \tau) = \sum_{j=0}^2 A_j(\xi, \eta) p_j(\tau), \quad (4.17)$$

$$D(\xi, \eta, \tau) = \sum_{l=0}^5 B_l(\xi, \eta) d_l(\tau), \quad (4.18)$$

where we have defined the following orthonormal basis to expand the population inversion:

$$B_0 = \sqrt{\pi} A_0^2, \quad B_1 = \sqrt{\pi} (A_1^2 - A_2^2),$$

$$B_2 = \sqrt{\pi} (A_1^2 + A_2^2 - A_0^2), \quad B_3 = \sqrt{2\pi} A_0 A_1,$$

$$B_4 = \sqrt{2\pi} A_0 A_2, \quad B_5 = \sqrt{4\pi} A_1 A_2. \quad (4.19)$$

We insert expansions (4.17) and (4.18) into Eqs. (4.8)–(4.10), leading to the following amplitude equations:

$$\partial_\tau e_j = -i\Omega_j e_j - \sigma_j e_j + p_j, \quad (4.20)$$

$$\partial_\tau p_0 = -(1+i\Delta)p_0 + \frac{1}{\sqrt{\pi}} \left[e_0 d_0 + \frac{1}{\sqrt{2}} (e_1 d_3 + e_2 d_4) \right], \quad (4.21)$$

$$\partial_\tau p_1 = -(1+i\Delta)p_1 + \frac{1}{\sqrt{\pi}} \left[\frac{1}{\sqrt{2}} e_0 d_3 + \frac{1}{2} (e_1 (d_0 + d_1 + d_2) + e_2 d_5) \right], \quad (4.22)$$

$$\partial_\tau p_2 = -(1+i\Delta)p_2 + \frac{1}{\sqrt{\pi}} \left[\frac{1}{\sqrt{2}} e_0 d_4 + \frac{1}{2} (e_2 (d_0 - d_1 + d_2) + e_1 d_5) \right], \quad (4.23)$$

$$\partial_\tau d_0 = -\gamma \left[d_0 - \sqrt{\pi} C + \frac{1}{2\sqrt{\pi}} \left(e_0^* p_0 + \frac{1}{2} (e_1^* p_1 + e_2^* p_2) + \text{c.c.} \right) \right], \quad (4.24)$$

$$\partial_\tau d_1 = -\gamma \left[d_1 + \frac{1}{4\pi} (e_1^* p_1 - e_2^* p_2^* + \text{c.c.}) \right], \quad (4.25)$$

$$\partial_\tau d_2 = -\gamma \left[d_2 - \sqrt{\pi} C + \frac{1}{4\sqrt{\pi}} (e_1^* p_1 + e_2^* p_2 + \text{c.c.}) \right], \quad (4.26)$$

$$\partial_\tau d_3 = -\gamma \left[d_3 + \frac{1}{2\sqrt{2\pi}} (e_0^* p_1 + e_1^* p_0 + \text{c.c.}) \right], \quad (4.27)$$

$$\partial_\tau d_4 = -\gamma \left[d_4 + \frac{1}{2\sqrt{2\pi}} (e_0^* p_2 + e_2^* p_0 + \text{c.c.}) \right], \quad (4.28)$$

$$\partial_\tau d_5 = -\gamma \left[d_5 + \frac{1}{4\sqrt{\pi}} (e_1^* p_2 + e_2^* p_1 + \text{c.c.}) \right]. \quad (4.29)$$

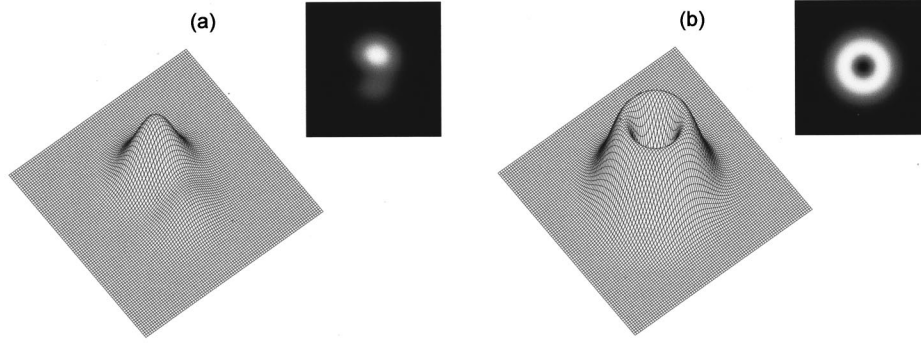


FIG. 11. Calculated transverse pattern intensity for $b = 11$ mm at times (a) $\tau \approx 180$ and (b) $\tau \approx 1000$. The real size of the picture is $5w_0 \times 5w_0$.

Using the same initial conditions indicated above, we have analyzed the small diaphragm ($b = 8$ mm) and large diaphragm ($b = 11$ mm) cases. In both cases all the parameters used are the same as the ones already used in the previous simulations. For the first case ($b = 8$ mm), the calculated results show that only the TEM_{00} mode is present during the interaction process. This is in agreement with the simulations presented in Sec. IV A, and also with the experimental patterns.

In the large aperture case ($b = 11$ mm) the simulated pattern evolution follows the same behavior as the corresponding one in Sec. IV A, in agreement with the experimental results. Indeed, the Gaussian mode grows during the gain-switch peak. After that, the TEM_{01} and TEM_{10} modes appear in the dynamics while the fundamental one decreases. Then, the intensity pattern displays a shifted peak [see Fig. 11(a)], followed by two symmetric peaks. This pattern rotates until the two peaks join together to display a doughnut mode [Fig. 11(b)].

The stationary regime of our system of equations can be studied provided that a pumping with a time duration much larger than the experimental one is utilized in our analysis. As expected, and in agreement with Brambilla *et al.* [3], we obtained an optical vortex rotating around the laser axis. This pattern is a traveling wave formed by the combination of the three considered modes (TEM_{00} , TEM_{01} , and TEM_{10}).

Then this simple method reproduces fairly well the experimental results, with an in-expensive computational cost. Therefore, this makes possible the use of even a modest personal computer to explore the stationary state.

V. EFFECT OF THE SPHERICAL MIRRORS

In order to study the role of the mirror's curvature in the observed dynamics, we now consider the Maxwell-Bloch equations for a flat mirror resonator, such that the curvature of the mirror included in the field equation (4.1) is neglected; in other words,

$$\frac{\partial E}{\partial \tau} = ia\Delta_{\perp} E - \sigma E + P. \quad (5.1)$$

We have integrated Eqs. (5.1), (4.2), and (4.3). To this end, we have selected a well-tested [15,16] linearly implicit finite-difference scheme because it is efficient and simple in both implementation and physical interpretation. The scheme uses a multigrid iterative algorithm to solve a linear system arising from the discretization of the transverse and temporal domain on a finite reticulum.

Simulations for $\mathcal{F} = 1.3$ and 2.1 were performed using $\Delta = 0.05$, $\kappa = 3.4 \times 10^7 \text{ s}^{-1}$, $\gamma_{\perp} = 2 \times 10^9 \text{ s}^{-1}$, and $\gamma_{\parallel} = 2 \times 10^6 \text{ s}^{-1}$. The results proved to be independent of the initial values of E and P , but dependent on the initial value of D , which was chosen to be a large-variance Gaussian.

The pump profile was uniformly distributed over the transverse plane, with a maximum value at the top of the pulse of $C_0 = 0.0236$. In agreement with previous sections, the time dependence of the pump was modeled as a pulse consisting of a fast rise time followed by a slow decay. The cylindrical cavity shape imposed by the diaphragm was modeled as two radially symmetric functions smoothly connected, which consist of a circular boundary with very high losses and a $(\tanh(\sqrt{x^2 + y^2}))$ function inside the circle delimited by the diaphragm.

Figures 12 and 13 show the calculated transient evolution of the transverse intensity profile for the two apertures investigated. While for $\mathcal{F} = 1.3$ the intensity distribution displays a bell-shaped pattern along the pulse duration (Fig. 12), for $\mathcal{F} = 2.1$ this pattern [see Fig. 13(a)] is momentarily suppressed by a short-lived doughnutlike structure [Fig. 13(b)].

The numerical results qualitatively agree with the experiments. Indeed, richer dynamics are observed when a large aperture is utilized, whereas only the fundamental mode survives when higher diffraction losses are produced by means of a smaller aperture [or a large value of the diffraction coefficient a in Eq. (5.1)]. Note, however, that in contrast to the experiments and the simulations performed in the case of a spherical mirror resonator, the evolution of the flat mirror resonator always displays cylindrical symmetry.

The curvature of the mirrors is thus a determining factor for the symmetry breaking to occur in our laser. The flat

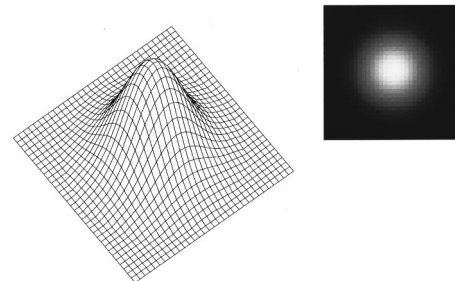


FIG. 12. Calculated transverse pattern intensity for $b = 8$ mm. A similar pattern is obtained during the whole pulse duration. The real size of the picture is $8 \times 8 \text{ mm}^2$.

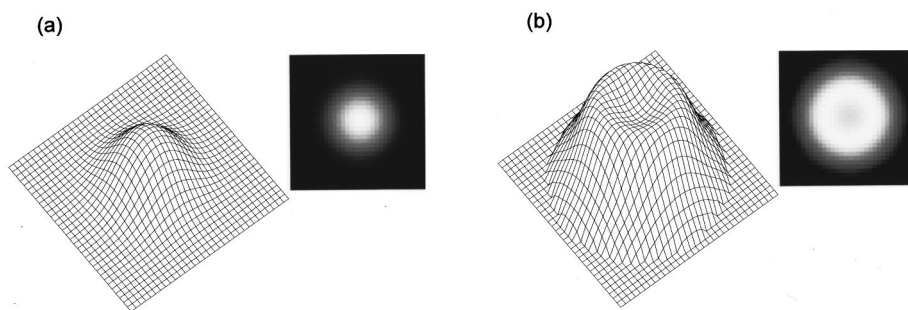


FIG. 13. Calculated transverse pattern intensity evolution for $b = 11$ mm. The real size of the picture is 11×11 mm².

mirror model is therefore inadequate to describe the evolution of the electromagnetic field in our laser resonator.

VI. CONCLUSIONS

In this paper an experimental and theoretical study of pattern evolution in pulsed atmospheric CO₂ lasers has been carried out. The fast pattern formation process has been directly measured with accurate spatiotemporal resolution. In spite of the intrinsic pattern simplicity, this study reveals rich dynamical processes hidden until now behind temporal averages. Interesting features observed when the experiment is performed with a large aperture are a spontaneous symmetry breaking and the lobes that are produced from this transition. Also worth mentioning is the dominance of a typical doughnut structure despite the low losses of the gaussian mode. Our study also comprised partially local intensity measurements with Fourier spectra characterized by a frequency beating corresponding to the TEM₀₀, TEM₁₀, and TEM₀₁ type structures. This observation, that can be considered as a result of the spatial structure of the cavity (formed by a couple of plane-concave mirrors), suggested the decomposition of the electric field in a superposition of these modes. A theoretical analysis along these lines was performed. The substitution of a linear combination of these modes in an electric field led to a system of coupled nonlinear differential equations of the mode amplitudes. The numerical solution of

the latter equations reproduced the experimentally measured results reasonably well, and gave a physical insight into the pattern dynamics. It also revealed that the doughnut mode, which arises when the TEM₁₀ and TEM₀₁ modes lock their phases, dominates the large aperture dynamics due to the spatial hole burning produced by the TEM₀₀ mode and the relatively low losses of the TEM₁₀ and TEM₀₁ modes, compared to the small aperture case. A different approach, based on an expansion of the matter variables, was shown to be a fast and simple method to solve the coupled system of equations. The results agreed remarkably with the previous theoretical analysis, and therefore with the experimental patterns. Finally, we eliminated the curvature term in the Maxwell-Bloch equations to analyze its effect. In this way, by means of a direct numerical integration we solved the Maxwell-Bloch equations of a flat mirror resonator. This model was not able to reproduce the entire temporal sequence experimentally registered, although it described some features of the simulated phenomenon qualitatively well. Therefore, these results show the relevance of the curvature of mirrors in the pattern evolution.

ACKNOWLEDGMENTS

We are very grateful to I. Martín for his helpful advice. This work was supported by the DGICYT under Project No. PB95-0389 (Spain).

-
- [1] F. Encinas-Sanz, J. M. Guerra, and I. Pastor, *Opt. Lett.* **21**, 1153 (1996).
 - [2] F. Prati, M. Brambilla, and L. A. Lugiato, *Riv. Nuovo Cimento* **17**, 1 (1994).
 - [3] M. Brambilla, M. Cattaneo, L. A. Lugiato, R. Pirovano, F. Prati, A. J. Kent, G. L. Oppo, A. B. Coates, C. O. Weiss, C. Green, E. J. D'Angelo, and J. R. Tredicce, *Phys. Rev. A* **49**, 1427 (1994).
 - [4] A. B. Coates, C. O. Weiss, C. Green, E. J. D'Angelo, J. R. Tredicce, M. Brambilla, M. Cattaneo, L. A. Lugiato, R. Pirovano, F. Prati, A. J. Kent, and G. L. Oppo, *Phys. Rev. A* **49**, 1452 (1994).
 - [5] D. V. Skryabin, *Quantum Semiclass. Opt.* **8**, 485 (1996).
 - [6] I. Boscolo, A. Bramati, M. Malvezzi, and F. Prati, *Phys. Rev. A* **55**, 738 (1996).
 - [7] E. Louvergneaux, D. Hennequin, D. Dangoisse, and P. Glorieux, *Phys. Rev. A* **53**, 4435 (1996).
 - [8] G. D'Alessandro and G. L. Oppo, *Opt. Commun.* **88**, 130 (1992).
 - [9] O. G. Calderón, V. M. Pérez-García, I. Martín, and J. M. Guerra, *Phys. Rev. A* **53**, 3490 (1996).
 - [10] F. Encinas-Sanz, J. Serna, C. Martínez, R. Martínez-Herrero, and P. M. Mejías, *IEEE J. Quantum Electron.* **34**, 1835 (1998).
 - [11] F. Encinas-Sanz and J. M. Guerra, *IEEE J. Quantum Electron.* **27**, 891 (1991).
 - [12] G. L. Oppo, G. D'Alessandro, and W. Firth, *Phys. Rev. A* **44**, 4712 (1991).
 - [13] K. Staliunas, M. F. H. Tarroja, and C. O. Weiss, *Opt. Commun.* **102**, 69 (1993).
 - [14] Chr. Tamm, and C. O. Weiss, *J. Opt. Soc. Am. B* **7**, 1034 (1990).
 - [15] I. Martín, V.M. Pérez-García, F. Tirado, and L. Vázquez, *Fluctuation Phenomena: Disorder and Nonlinearity*, edited by A. R. Bishop, S. Jiménez, and L. Vázquez (World Scientific, Singapore, 1995), p. 390.
 - [16] B. Guo, I. Martín, V. M. Pérez-García, and L. Vázquez, *J. Comput. Phys.* **129**, 181 (1996).